Spiro-Linked Molecular Hole-Transport Materials for Highly Efficient Inverted Perovskite Solar Cells

Chuan Wang, Jinlong Hu, Chaohui Li, Shudi Qiu, Xianhu Liu,* Linxiang Zeng, Chuntai Liu, Yaohua Mai,* and Fei Guo*

Spiro-linked compounds have been used as benchmark hole-transport materials (HTMs) for the construction of efficient normal architecture (n-i-p) perovskite solar cells (PSCs). However, the heavy reliance on the use of dopants not only complicates the device fabrication but imposes long-term stability concern of the devices. Herein, it is reported that solution-processed dopant-free spiro molecules can serve as superior HTMs to fabricate efficient inverted (p-i-n) PSCs. Rational choice of orthogonal solvent allows us to solution deposit uniform and pinhole-free perovskite films without compromising the hole-extraction capability of the spiro-based interface layers. To illustrate the generality of the strategy, three spiro-linked molecules are investigated side by side as HTMs in one-step solution-processed CH$_3$NH$_3$PbI$_3$ PSCs. Due to the favored energy-level alignment and high hole mobility, solar cells based on the HTM of spiro-TTB yield a high efficiency of 18.38% with open-circuit voltages (V_{OC}) up to 1.09 V. These results suggest that small molecular HTMs commonly developed for normal structure devices can be of great potential to fabricate cost-effective and highly efficient inverted PSCs.

1. Introduction

Organometal halide perovskite solar cells (PSCs) have attracted intensive research attention as a promising solar technology due to their superb photovoltaic performance and potentially low production cost.[1–4] The rapid development of the perovskite solar technology was enabled by the tremendous effort in designing perovskite compositions, developing versatile solution deposition technologies, and optimizing the morphology of perovskite layer.[5–10] The combination of these efforts has pushed the power conversion efficiency (PCE) of PSCs to an impressive level of 25.2% within a decade.[11–15] Typically, PSCs can be constructed in either a normal structure (n-i-p) or an inverted (p-i-n) structure, depending on the extraction direction of charge carriers.[16] For both types of devices, apart from preparing a defect-less perovskite absorber layer to suppress nonradiative recombination, selectively extracting photogenerated charge carriers toward electrical contacts plays a determinative role in achieving highly efficient devices.

Hole-transport layers (HTLs) take the role of extracting holes and blocking electrons, thus strongly influencing charge recombination at the interfaces.[17–20] Among a wide variety of hole-transport materials (HTMs) reported in the literature, conjugated small molecules based on spiro unit have been demonstrated as state-of-the-art workhorse HTMs for fabrication of high-performance PSCs.[21,22] The unique characteristics of the spiro-based materials originate from their rigid structures conferring high thermal stability and the appropriate energy levels for transferring holes and blocking electrons.[23] The most successful application of the spiro-based materials was implemented as HTLs in normal (n-i-p) architecture devices, which necessarily requires a thick film of around 200–300 nm to fully cover the perovskite layer underneath.[21] However, it is noticeable that pristine spiro-based materials without doping are unqualified in delivering highly efficient PSCs.[24] This is primarily because the low conductivity of the undoped spiro-based materials can result in large internal series resistance.[24–26] As a consequence, normal structure PSCs prepared with undoped spiro HTMs generally exhibited a rather low fill factor (FF) and open-circuit voltage (V_{OC}).[27] A generally accepted solution to enhance the conductivity of spiro-based thin films is doping with inorganic salt or small molecules such as lithium bis(trifluoromethanesulfonyl) imide and 4-*tert*-butylpyridine (tBP).[21,28,29] Unfortunately, the presence of these chemical dopants can promote ion migration at the electrical field and deteriorate long-term stability of the devices.[17,30] Moreover, the incorporation of these exotic additive inevitably increases the fabrication cost. In this context, it is of great importance that dopant-free spiro-based

C. Wang, Dr. J. Hu, C. Li, S. Qiu, Prof. Y. Mai, Dr. F. Guo
Institute of New Energy Technology
College of Information Science and Technology
Jinan University
Guangzhou 510632, China
E-mail: yaohuamai@jnu.edu.cn; fei.guo@jnu.edu.cn

C. Wang, C. Li, Prof. X. Liu, Prof. C. Liu
National Engineering Research Center for Advanced Polymer Processing Technology
Zhengzhou University
Zhengzhou 450002, China
E-mail: xianhu.liu@zzu.edu.cn

L. Zeng
Department of Materials Science and Engineering
Zhejiang University
Hangzhou 310027, China

The ORCID identification number(s) for the author(s) of this article can be found under https://doi.org/10.1002/solr.201900389.

materials can be used as HTLs to construct PSCs with enhanced stability and low production cost.

In this work, we demonstrate that spiro-based hole-transport molecules, which are overwhelmingly used in normal architecture devices, can be worked upon as superior HTMs to fabricate efficient inverted PSCs. We first resolved the most intractable processing challenge by careful selection of solvent for the preparation of perovskite solution. This is a decisive step that enables the sequential deposition of the spiro HTMs and the subsequent perovskite layer on top via entirely solution processing. Three types of spiro-based materials were investigated side by side to identify the potential of these small molecules for construction of inverted PSCs. It is found that the photovoltaic performance of the devices is strongly correlated with the energetic alignment between the HTMs and perovskite. The favorably aligned energy levels of spiro-TTB with the perovskite in combination with its high hole mobility result in substantially reduced interfacial recombination. As a result, the spiro-TTB-based solar cells demonstrated the highest V_{OC} of up to 1.09 V, leading to a PCE of 18.38%.

2. Results and Discussion

Three types of triphenylamine derivatives with the spiro core were used as HTMs in the present study: 2,2′,7,7′-tetra (N,N-di-tolyl)amino-9,9-spirobifluorene (spiro-TTB), 2,2′,7,7′-tetrakis-(diphenylamino)-9,9′-spirobifluorene (spiro-TAD), and 2,2′,7,7′-tetrakis[N,N-di(4-methoxyphenyl)amino]-9,9′-spirobifluorene (spiro-MeOTAD). The chemical structures of the three molecules are shown in **Figure 1**. These materials were selected mainly due to their high hole mobilities and high visible transparency, which have been studied in the field of organic electronics.[23,31] It is further expected that maintaining structural similarity would preclude interface compatibility that may influence the processability and morphology of the top perovskite layer. As indicated in Figure S1, Supporting Information, all the three molecules show high transmittance in the entire visible range, making them ideal candidates for the construction of solar cells in terms of negligible absorption losses. The hole mobility of the three molecules was determined using the space charge limited current (SCLC) method with the results plotted in Figure S2, Supporting Information, and **Table 1**. It is found that the spiro-TTB exhibits a superior hole mobility of $1.97 \times 10^{-3} \, \mathrm{cm^2 \, V^{-1} \, s^{-1}}$ which is about four times higher than that of spiro-TAD ($4.73 \times 10^{-4} \, \mathrm{cm^2 \, V^{-1} \, s^{-1}}$) and an order of magnitude higher than that of spiro-MeOTAD ($1.96 \times 10^{-4} \, \mathrm{cm^2 \, V^{-1} \, s^{-1}}$). Considering that the organic interface layer in inverted PSCs requires only a film thickness from few to tens of nanometers, a mobility higher than $1 \times 10^{-5} \, \mathrm{cm^2 \, V^{-1} \, s^{-1}}$ is sufficient to vertically transport charge carriers toward the anode without resistance losses.

It is known that the surface energy of the interface layers plays a crucial role in determining the solution processability and crystal morphology of the perovskite thin films.[5,32] We therefore first examined the surface wettability of the spiro-based small molecules using water contact angle measurement. As shown in Figure 1, all the three spiro-based small molecules show hydrophilic surface properties with water contact angles smaller than 90°. The low surface energies of the spiro molecule films enable facile deposition of perovskite film via solution processing.

During device fabrication, we observed that although dense and uniform perovskite films with high specularity can be deposited on spiro HTLs, the prepared solar cells did not deliver satisfactory photovoltaic performance. We have therefore conducted a thorough optimization, but in vain, to exclude the possible influence factors that hamper the device performance, such as thickness of the HTLs, morphology, and crystallinity of

Table 1. Photovoltaic parameters of the best-performing inverted PSCs deposited on the three types of spiro-based molecular HTMs (reverse scan).

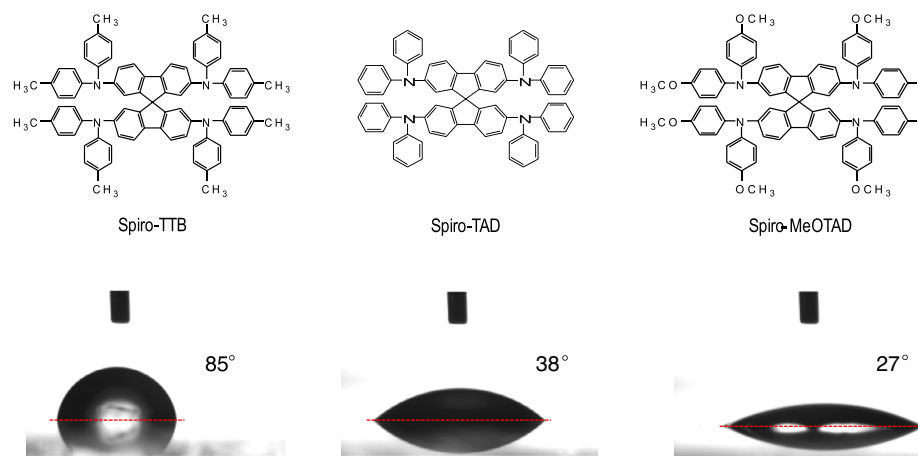| HTM	HOMO [eV]	Mobility [cm² V⁻¹ s⁻¹]	V_{OC} [V]	J_{SC} [mA cm⁻²]	FF [%]	PCE [%]
Spiro-TTB	5.30	1.97×10^{-3}	1.07	22.02	78	18.38
Spiro-TAD	5.41	4.73×10^{-4}	0.99	21.57	76	16.23
Spiro-MeOTAD	5.05	1.96×10^{-4}	0.99	22.03	73	15.92
W/O	4.70	–	0.94	12.63	53	6.29

Figure 1. Chemical structures of the spiro-based HTMs and the corresponding water contact angle measurement.

the perovskite films. Eventually, we found out that these spiro-based small molecules, which are processed from chlorobenzene, can be readily dissolved in dimethylformamide (DMF), which is the commonly used solvent for perovskite solution preparation (Figure S3, Supporting Information). The easy dissolution of the spiro-based molecules in DMF poses a processing challenge that the predeposited spiro-based HTMs can be washed away during solution coating of the top perovskite layer. To bypass this drawback, very few works have previously managed to deposit perovskite on spiro HTLs by vacuum process, where the spiro compounds and perovskites were sequentially deposited via thermal evaporation.[33–35] Unfortunately, these vacuum-processed inverted PSCs showed fairly low device performance.

In the present work, we sought to achieve an entirely solution process to exploit the full potential of these spiro-linked small molecules for the construction of inverted PSCs. The observation of dissolubility of the spiro molecules in DMF encourages us to search for orthogonal solvent to deposit perovskite layer. Previous works have shown that apart from the widely used solvent mixture of DMF and dimethyl sulfoxide (DMSO) for perovskite precursor preparation, the combination of gamma-butyrolactone (GBL) and DMSO was also capable of producing efficient PSCs.[3,36] Fortunately, it is observed that all the three spiro molecules can be hardly dissolved in the binary solvent consisting of GBL and DMSO (Figure S3, Supporting Information). The use of orthogonal solvent for depositing the perovskite layer guarantees to preserve the optoelectronic properties of the underlying spiro-based HTL.

Having found the favored solvent for perovskite precursor which is immiscible to the underlying spiro-based small molecules, we constructed inverted PSCs with a device architecture of ITO/spiro molecule/perovskite/PCBM/BCP/Ag (Figure 2a). A typical cross-sectional scanning electron microscopy (SEM) image of the prepared perovskite devices is shown in Figure 2b, where a thin layer of the organic spiro-TTB sandwiched between indium tin oxide (ITO) and perovskite is clearly seen. Notably, the perovskite layer comprises mainly vertically aligned grains throughout the device, which is beneficial for charge transport with minimal recombination at grain boundaries.

The energy band diagram of the device stack is schematically shown in Figure 2c, where the highest occupied molecular orbital (HOMO) levels of the spiro-based HTMs were determined by ultraviolet photoelectron spectroscopy (UPS) (Figure S4,

Supporting Information).[37,38] The lowest unoccupied molecular orbital (LUMO) potentials of the molecules were calculated from $(E_{HOMO} - E_{Bandgap})$ (Figure S5, Supporting Information). From Figure 2c, one can see that all the three spiro HTLs possess HOMO levels close to the valence band (VB) of the perovskite. In particular, the cascade energy-level alignment between the HOMO of spiro-TTB with the VB of perovskite facilitates efficient hole extraction, which is beneficial for delivering high photovoltage and current density. In contrast, the spiro-MeOTAD exhibits a HOMO level of 5.05 eV, which is 0.45 eV higher than the VB of perovskite. The high HOMO level of the spiro-MeOTAD close to the conduction band of the perovskite is detrimental to device performance due to the high probability of recombination of the holes at the HOMO of spiro-MeOTAD with the electrons hopped to the conduction band of the perovskite.

Figure 3 shows the current density–voltage (J–V) characteristics of the best-performing solar cells based on the three spiro-based HTMs. The solar cells were measured under standard AM 1.5G illumination with an intensity of 100 mW cm^{-2}. The corresponding photovoltaic parameters are shown in Table 1.
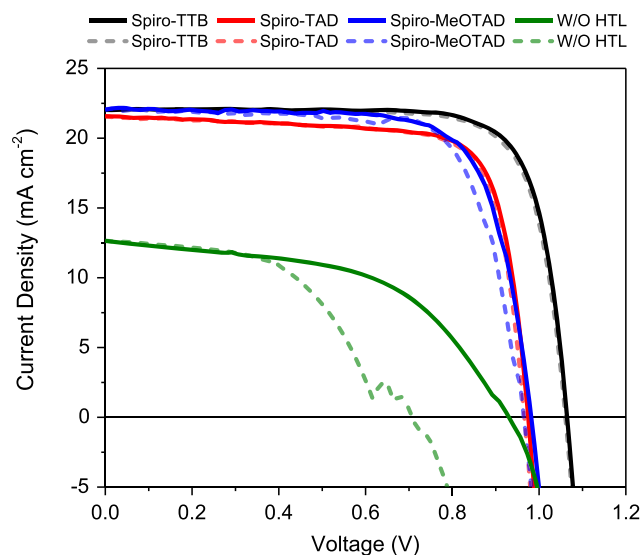
Figure 3. J–V characteristics of the best-performing PSCs with the three spiro-based HTMs. The solid and dashed lines stand for the J–V curves scanned from reverse and forward, respectively.
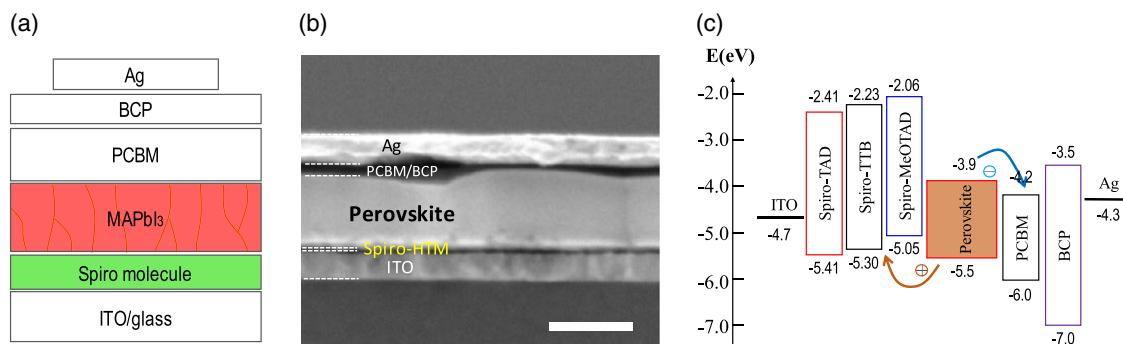
Figure 2. a) Schematic structure of the solar cell stack. b) Cross-sectional SEM image of a complete solar cell device. The scale bar is 500 nm. c) Energy diagram of the device with spiro-linked compounds as HTLs.

The spiro-TTB-based solar cell shows a PCE of up to 18.38% with a high V_{OC} of 1.07 V, an FF of 78%, and a current density (J_{SC}) of 22.02 mA cm^{-2}. It is worth noting that the obtained PCE of 18.38% is among the highest efficiencies for inverted PSCs based on small molecular HTMs (Figure S6, Supporting Information).[39–43] The solar cells based on the HTMs of spiro-TAD and spiro-MeOTAD show decent PCEs of ≈16% and relatively low V_{OC} values of 0.99 V. For comparison, a typical control device without HTL exhibits a rather inferior PCE of only 6.29%, with a V_{OC} of 0.94 V, a J_{SC} of 12.63 mA cm^{-2}, and an FF of 53%. More importantly, the spiro-HTM-based solar cells exhibited significantly suppressed J–V hysteresis behavior as compared with the control device, indicating efficient charge exaction by these spiro-based interface materials without significant charge accumulation at interfaces.[44,45] To illustrate the repeatability of the devices, more than 20 devices for each HTMs were fabricated. As shown in Figure S7, Supporting Information, the narrow distribution of the photovoltaic parameters demonstrated good reproducibility of these inverted PSCs based on the HTMs of spiro molecules. In sum, these results underline that spiro-based small molecules, particularly spiro-TTB, are promising small molecular HTMs in delivering high-performance inverted PSCs.

It is observed that the solar cells based on spiro-TTB exhibited the highest PCE among the three solar cells. It is further noticed that the high device performance of spiro-TTB mainly originates from the high V_{OC} of 1.09 V which is ≈100 mV larger than the other two spiro-based devices (Figure S7, Supporting Information). To uncover the origin of the difference in device performance, we first scrutinized the morphology properties of the perovskite films deposited on the three spiro-based HTMs. SEM images in **Figure 4**a–c show that all the three perovskite films have similar crystal sizes in the range of 100–400 nm with full surface coverage (Figure S8, Supporting Information). The surface roughness of the perovskite films was determined by atomic force microscopy (Figure S9, Supporting Information), which gives root mean square (RMS) roughness values of 11.8, 11.6, and 8.7 nm for the spiro-TTB, spiro-TAD, and spiro-MeOTAD, respectively. These observations suggest that although the three spiro molecules have different surface energies, the crystal morphology of the perovskite films is not significantly affected.

We further investigated the crystal structure of the perovskite films using X-ray diffraction (XRD) spectroscopy. It is found that the three perovskite films deposited on the spiro layers show the characteristics of the perovskite crystal structure (Figure 4d), where the diffraction peaks at 14.1° and 28.4° are indexed to the (110) and (220) planes, respectively. The presence of the two sharp peaks with similar intensity indicates that the polycrystalline perovskites deposited on the three spiro HTMs possess similar high crystallinity and preferential crystal orientations (also see Figure S10, Supporting Information). In addition, small diffraction peaks located at ≈12.7° are observed in the three films, which can be assigned to the (001) plane of the PbI_2 crystal. It has been reported that the presence of a small amount of PbI_2 is beneficial for reducing hysteresis and ionic migration due to surface defects passivation.[46–48] Overall, the film morphology and crystal structure surveys confirm that the quality of $MAPbI_3$ films grown on the three spiro-based small molecules is almost identical.

We now turn to probe the charge transfer dynamics at the interface of perovskite/spiro-based HTMs using steady-state photoluminescence (PL) and time-resolved photoluminescence (TRPL). **Figure 5**a shows the PL emission spectra of the perovskite deposited on the three types of spiro molecules. It is shown that the perovskite deposited on bare glass substrate exhibited a predominant PL emission centered at 782 nm, which is representative for $MAPbI_3$. Distinctly, the PL intensity of the perovskite film on spiro-TTB is substantially quenched, confirming that spiro-TTB facilitates efficient hole extraction and transport from perovskite to the HTL. By contrast, the PL emissions of the other
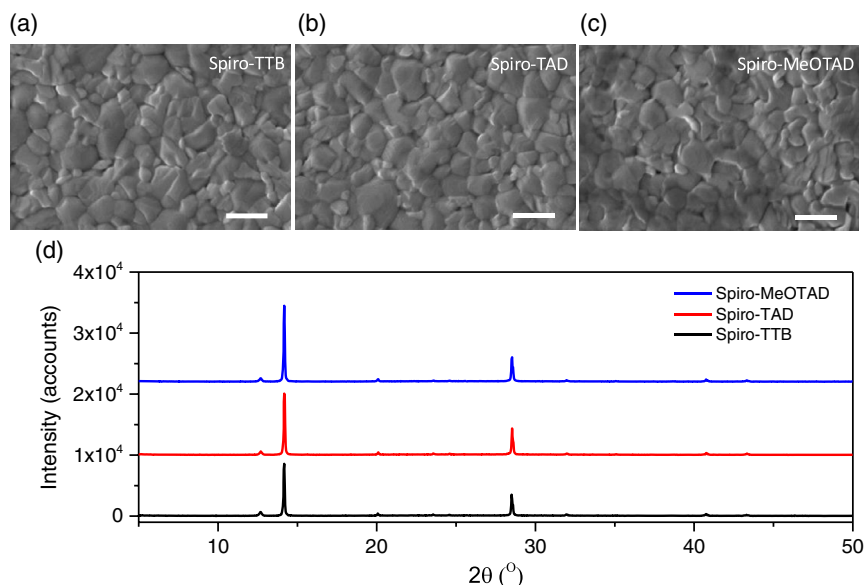

Figure 4. SEM images of the $MAPbI_3$ perovskite films deposited on the spiro HTM-coated ITO/Glass substrate: a) spiro-TTB, b) spiro-TAD, c) spiro-MeOTAD, and d) the corresponding XRD spectra. Scale bars are 500 nm.
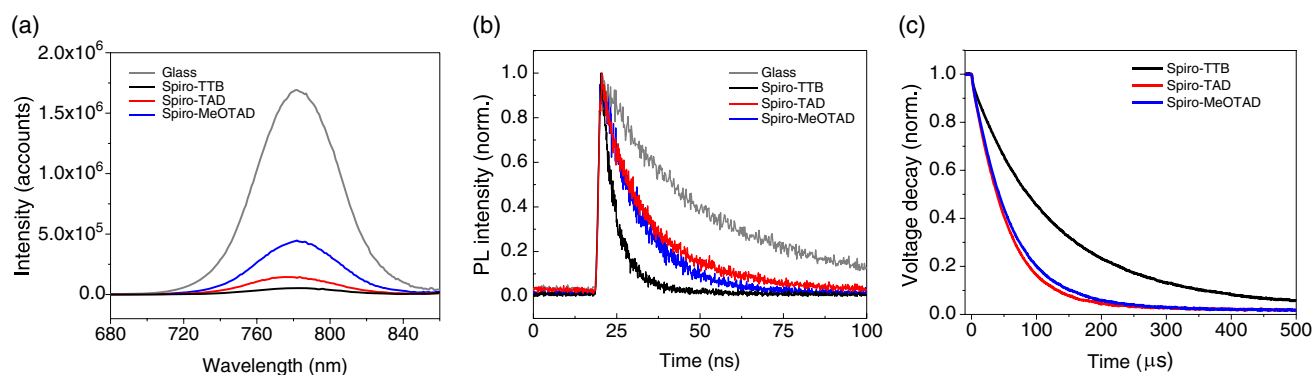
Figure 5. a) Steady-state PL spectra and b) PL decay spectra of the perovskite films deposited on the spiro molecules-coated ITO/glass substrates. c) TPV characteristic of the solar cells operated at open-circuit conditions.

two spiro-based molecules are less significantly quenched. Figure 5b shows the commensurate TRPL characteristics, which were measured by exciting the samples with a 470 nm pulsed laser. The derived carrier lifetimes (τ) fitted by the single exponential decay yields lifetime constants of 32.6, 13.6, 11.7, and 4.7 ns for the perovskite films deposited on glass, spiro-MeOTAD, spiro-TAD, and spiro-TTB, respectively. The shortest decay time of the perovskite/sprio-TTB based film (4.7 ns) further validates the most efficient hole-extraction capability of spiro-TTB, which is consistent with the steady-state PL results.

Transient photovoltage (TPV) decay was further recorded to understand the interfacial charge recombination within the solar devices.[49] During the TPV measurement, the solar cells were illuminated with a constant light intensity for a period of time to reach a photostationary state and then the light was suddenly switched off and voltage decay was recorded over time. Since the solar cell is operated at an open circuit, the voltage decay reflects the recombination behavior of the photon-generated charge carriers in the device. As shown in Figure 5c, the spiro-TTB-based solar cell shows a decay time lifetime (τ_r) of 135 μs which is noticeably longer than that of the spiro-TAD ($\tau_r = 57$ μs)- and spiro-MeOTAD ($\tau_r = 63$ μs)-based devices. The longer decay constant indicates slower charge recombination at the interfaces, which should be the main factor responsible for the high V_{OC} of the spiro-TTB-based solar cells.

Lastly, we also fabricated a solar cell using doped spiro-TTB as the HTMs to assess whether doping the HTM is necessary in inverted devices. It is seen from Figure S11, Supporting Information, that, compared with the device-based HTL of pristine spiro-TTB, the solar cell based on doped spiro-TTB possesses similar V_{OC} and J_{SC} values (Table S1, Supporting Information). The lower efficiency of 14.54% mainly results from the lower FF of 63%, which is likely due to the dopant-induced interfacial charge recombination. These results suggest that undoped small-molecular HTLs could outperform their doped counterparts in delivering high-efficiency inverted PSCs.

3. Conclusions

In summary, we have demonstrated that solution-processed spiro-linked compounds are highly promising HTMs for fabricating efficient inverted PSCs. Through judicious solvent engineering of the perovskite ink, dense and uniform perovskite thin films were deposited on top of the spiro HTLs without compromising the optoelectronic properties. The general application of the method was illustrated by investigating three spiro-linked compounds as HTMs in MAPbI$_3$ solar cells. The results suggest that spiro-TTB-based inverted devices exhibited a high PCE of 18.38% and a V_{OC} value of up to 1.09 V, primarily due to the suppressed interfacial charge recombination as a result of favorable energy-level alignment. These results established an alternative approach to fabricate efficient inverted PSCs using both existing and newly developed small molecules that are aiming for the construction of normal structure PSCs.

4. Experimental Section

Materials and Solution Preparation: Lead iodide (PbI$_2$, 99.9985%) was purchased from Alfa Aesar. Methylammonium iodide (MAI) was purchased from Xi'an p-OLED Co. Spiro-MeOTAD (>99%), spiro-TTB (>99%), bathocuproine (BCP), and PC$_{61}$BM were purchased from Lumtec. Spiro-TAD (>98%) was obtained from Macklin. Methylammonium chloride (MACl, 98%) and all the solvents were purchased from Sigma-Aldrich. All the chemicals were used as received without further purification.

Perovskite precursor solution was prepared by dissolving 1 M equimolar ratio of PbI$_2$ and MAI in a mixed solvent of GBL and DMSO (volume ratio 7:3). In the precursor solution, MACl (10% molar ratio) was added as the morphology modulator to realize the dense and uniform perovskite film. The doped spiro-TTB solution was prepared as follows: 5 mg spiro-TTB was dissolved in 0.97 mL chlorobenzene followed by adding 9.6 uL 4-tBP and 36.7 uL lithium bis(trifluoromethanesulfonyl)imide (Li-TFSI) solution (56.7 mg LI-TSFI in 1 mL acetonitrile) into the spiro-TTB solution. Then, 12.5 uL FK102 (86.7 mg FK102 in 1 mL acetonitrile) was added to the tBP and Li-TFSI-doped spiro-TTB solution.

Solar Cell Fabrication: The prepatterned ITO-coated glass (OPV Tech Co., Ltd.) substrates were sequentially cleaned by sonicating the substrates in acetone and isopropanol for 10 min each. On the cleaned ITO substrate, spiro-based HTM was spin coated from 5 mg mL^{-1} chlorobenzene solution at 5000 rpm for 30 s, which was annealed at 120 °C for 10 min in ambient air. The layer thickness of the sipiro-based molecules was below 10 nm, which was too thin to be precisely determined by step profiler and cross-sectional SEM imaging. After it cooled down to room temperature, the substrate was transferred to a nitrogen-filled glovebox. The MAPbI$_3$ perovskite layer was subsequently deposited by the vacuum-assisted blade-coating method, as described in our previous work.[50]

The only difference is that the solvent used in this work was GBL:DMSO (7:3 vol%) instead of the DMF:DMSO (4:1 vol%). On top of the perovskite film, electro-transporting layer of $PC_{61}BM$ (15 mg mL^{-1} in chlorobenzene) and the interfacial layer BCP (2.5 mg mL^{-1} in isopropanol) were successively deposited by spin coating at 2000 rpm for 30 s and 5000 rpm for 30 s, respectively. Finally, a 120 nm Ag metal electrode was thermally evaporated to complete the devices. The active area of the solar cells was 0.09 cm^2, which was determined by the overlapping between the top Ag and bottom ITO electrode. All the films and solar devices were characterized without encapsulation.

Characterizations: The crystal structure was characterized by a Bruker D8 Advance X-ray diffractometer with CuKα radiation operated at 40 kV and 40 mA. The surface microstructure and cross-sectional morphology of the solar cells were imaged by field-emission SEM (FEI Apreo LoVac). UPS measurements were performed using a Thermo Scientific K-Alpha with an He I (21.2 eV) excitation source at an ultrahigh vacuum of 1.0×10^{-10} Torr. PL and time-resolved PL decay were recorded with a spectrophotometer (Gilden Photonics) using a pulsed source at 470 nm (Ps diode lasers BDS-SM). A double-beam spectrophotometer (Lambda 950, PerkinElmer) equipped with an integrated sphere was used for the UV–vis absorption measurement. The water contact angle was obtained using a Micro Capture Pro coupled with ImageJ software. Current density–voltage (*J–V*) characteristics of the solar cells were measured using a Keithley 2400 source meter. The illumination was provided by a Newport Oriel 92192 solar simulator with an AM 1.5G filter, operating at 100 mW cm^{-2}, which was calibrated by a standard silicon solar cell from Newport. Both forward and backward scans were performed, and the scan speed was fixed at 0.15 V s^{-1}. The TPV decay measurements were performed on an electrochemical workstation (ZAHNER, Germany).

Supporting Information

Supporting Information is available from the Wiley Online Library or from the author.

Acknowledgements

Conflict of Interest

The authors declare no conflict of interest.

Keywords

[1] M. Gratzel, *Nat. Mater.* **2014**, *13*, 838.
[2] M. A. Green, A. Ho-Baillie, H. J. Snaith, *Nat. Photonics* **2014**, *8*, 506.
[3] N. J. Jeon, J. H. Noh, Y. C. Kim, W. S. Yang, S. Ryu, S. I. Seok, *Nat. Mater.* **2014**, *13*, 897.
[4] Z. Li, T. R. Klein, D. H. Kim, M. J. Yang, J. J. Berry, M. F. A. M. van Hest, K. Zhu, *Nat. Rev. Mater.* **2018**, *3*, 18017.
[5] C. Bi, Q. Wang, Y. C. Shao, Y. B. Yuan, Z. G. Xiao, J. S. Huang, *Nat. Commun.* **2015**, *6*, 7747.
[6] P. Schulz, *ACS Energy Lett.* **2018**, *3*, 1287.
[7] J. Lee, H. Kang, G. Kim, H. Back, J. Kim, S. Hong, B. Park, E. Lee, K. Lee, *Adv. Mater.* **2017**, *29*, 1606363.
[8] F. Guo, W. X. He, S. D. Qiu, C. Wang, X. H. Liu, K. Forberich, C. J. Brabec, Y. H. Mai, *Adv. Funct. Mater.* **2019**, *29*, 1900964.
[9] G. X. Liang, P. Fan, J. T. Luo, D. Gu, Z. H. Zheng, *Prog. Photovoltaics* **2015**, *23*, 1901.
[10] L. Zeng, Z. Chen, S. Qiu, J. Hu, C. Li, X. Liu, G. Liang, C. J. Brabec, Y. Mai, F. Guo, *Nano Energy* **2019**, *66*, 104099.
[11] A. Kojima, K. Teshima, Y. Shirai, T. Miyasaka, *J. Am. Chem. Soc.* **2009**, *131*, 6050.
[12] J. Burschka, N. Pellet, S. J. Moon, R. Humphry-Baker, P. Gao, M. K. Nazeeruddin, M. Gratzel, *Nature* **2013**, *499*, 316.
[13] Z. G. Xiao, C. Bi, Y. C. Shao, Q. F. Dong, Q. Wang, Y. B. Yuan, C. G. Wang, Y. L. Gao, J. S. Huang, *Energy Environ. Sci.* **2014**, *7*, 2619.
[14] B. Conings, A. Babayigit, M. T. Klug, S. Bai, N. Gauquelin, N. Sakai, J. T. W. Wang, J. Verbeeck, H. G. Boyen, H. J. Snaith, *Adv. Mater.* **2016**, *28*, 10701.
[15] X. Li, D. Q. Bi, C. Y. Yi, J. D. Decoppet, J. S. Luo, S. M. Zakeeruddin, A. Hagfeldt, M. Gratzel, *Science* **2016**, *353*, 58.
[16] A. N. Cho, N. G. Park, *ChemSusChem* **2017**, *10*, 3687.
[17] S. Ameen, M. A. Rub, S. A. Kosa, K. A. Alamry, M. S. Akhtar, H. S. Shin, H. K. Seo, A. M. Asiri, M. K. Nazeeruddin, *ChemSusChem* **2016**, *9*, 10.
[18] Z. Yu, L. C. Sun, *Adv. Energy Mater.* **2015**, *5*, 1500213.
[19] W. X. Zhang, Y. C. Wang, X. D. Li, C. J. Song, L. Wan, K. Usman, J. F. Fang, *Adv. Sci.* **2018**, *5*, 1800159.
[20] W. Chen, F. Z. Liu, X. Y. Feng, A. B. Djurisic, W. K. Chan, Z. B. He, *Adv. Energy Mater.* **2017**, *7*, 1700722.
[21] Z. Hawash, L. K. Ono, Y. B. Qi, *Adv. Mater. Interfaces* **2018**, *5*, 1800159.
[22] T. S. Su, H. Y. Tsai, K. Kannankutty, C. T. Chen, Y. Chi, T. C. Wei, *Sol. RRL* **2019**, *3*, 1900143.
[23] T. P. Saragi, T. Fuhrmann-Lieker, J. Salbeck, *Adv. Funct. Mater.* **2006**, *16*, 966.
[24] W. Q. Zhou, Z. H. Wen, P. Gao, *Adv. Energy Mater.* **2018**, *8*, 1702512.
[25] A. Abate, T. Leijtens, S. Pathak, J. Teuscher, R. Avolio, M. E. Errico, J. Kirkpatrik, J. M. Ball, P. Docampo, I. McPherson, H. J. Snaith, *Phys. Chem. Chem. Phys.* **2013**, *15*, 2572.
[26] L. K. Ono, P. Schulz, J. J. Endres, G. O. Nikiforov, Y. Kato, A. Kahn, Y. B. Qi, *J. Phys. Chem. Lett.* **2014**, *5*, 1374.
[27] M. Cheng, C. Chen, B. Xu, Y. Hua, F. G. Zhang, L. Kloo, L. C. Sun, *J. Energy Chem.* **2015**, *24*, 698.
[28] Y. K. Wang, Z. C. Yuan, G. Z. Shi, Y. X. Li, Q. Li, F. Hui, B. Q. Sun, Z. Q. Jiang, L. S. Liao, *Adv. Funct. Mater.* **2016**, *26*, 1375.
[29] Z. Hawash, L. K. Ono, Y. B. Qi, *Adv. Mater. Interfaces* **2016**, *3*, 1600117.
[30] L. Calio, S. Kazim, M. Gratzel, S. Ahmad, *Angew. Chem., Int. Ed.* **2016**, *55*, 14522.
[31] J. Salbeck, N. Yu, J. Bauer, F. Weissörtel, H. Bestgen, *Synth. Met.* **1997**, *91*, 209.
[32] J. You, F. Guo, S. Qiu, W. He, C. Wang, X. Liu, W. Xu, Y. Mai, *J. Energy Chem.* **2019**, *38*, 192.
[33] L. E. Polander, P. Pahner, M. Schwarze, M. Saalfrank, C. Koerner, K. Leo, *APL Mater.* **2014**, *2*, 081503.
[34] E. Erdenebileg, L. E. Scholz, A. Hofacker, C. Koerner, K. Leo, *Energy Technol.* **2017**, *5*, 1606.
[35] F. Sahli, J. Werner, B. A. Kamino, M. Brauninger, R. Monnard, B. Paviet-Salomon, L. Barraud, L. Ding, J. J. D. Leon, D. Sacchetto, G. Cattaneo, M. Despeisse, M. Boccard, S. Nicolay, Q. Jeangros, B. Niesen, C. Ballif, *Nat. Mater.* **2018**, *17*, 820.

[36] M. J. Yang, Z. Li, M. O. Reese, O. G. Reid, D. H. Kim, S. Siol, T. R. Klein, Y. Yan, J. J. Berry, M. F. A. M. van Hest, K. Zhu, *Nat. Energy* **2017**, *2*, 17038.

[37] Z. Hawash, L. K. Ono, S. R. Raga, M. V. Lee, Y. B. Qi, *Chem. Mater.* **2015**, *27*, 562.

[38] S. H. Wang, T. Sakurai, W. J. Wen, Y. B. Qi, *Adv. Mater. Interfaces* **2018**, *5*, 1800260.

[39] C. Y. Huang, W. F. Fu, C. Z. Li, Z. Q. Zhang, W. M. Qiu, M. M. Shi, P. Heremans, A. K. Y. Jen, H. Z. Chen, *J. Am. Chem. Soc.* **2016**, *138*, 2528.

[40] L. Y. Yang, F. L. Cai, Y. Yan, J. H. Li, D. Liu, A. J. Pearson, T. Wang, *Adv. Funct. Mater.* **2017**, *27*, 1702613.

[41] Y. Wang, W. Chen, L. Wang, B. Tu, T. Chen, B. Liu, K. Yang, C. W. Koh, X. H. Zhang, H. L. Sun, G. C. Chen, X. Y. Feng, H. Y. Woo, A. B. Djurisic, Z. B. He, X. G. Guo, *Adv. Mater.* **2019**, *31*, 1902781.

[42] Y. Chen, X. Xu, N. Cai, S. Qian, R. Luo, Y. Huo, S. W. Tsang, *Adv. Energy Mater.* **2019**, 1901268.

[43] R. A. Belisle, P. Jain, R. Prasanna, T. Leijtens, M. D. McGehee, *ACS Energy Lett.* **2016**, *1*, 556.

[44] B. Wu, K. W. Fu, N. Yantara, G. C. Xing, S. Y. Sun, T. C. Sum, N. Mathews, *Adv. Energy Mater.* **2015**, *5*, 1500829.

[45] S. Rayishankar, S. Gharibzadeh, C. Roldan-Carmona, G. Grancini, Y. Lee, M. Ralaiarisoa, A. M. Asiri, N. Koch, J. Bisquert, M. K. Nazeeruddin, *Joule* **2018**, *2*, 788.

[46] F. Liu, Q. Dong, M. K. Wong, A. B. Djurišić, A. Ng, Z. Ren, Q. Shen, C. Surya, W. K. Chan, J. Wang, *Adv. Energy Mater.* **2016**, *6*, 1502206.

[47] Y. C. Kim, N. J. Jeon, J. H. Noh, W. S. Yang, J. Seo, J. S. Yun, A. Ho-Baillie, S. Huang, M. A. Green, J. Seidel, *Adv. Energy Mater.* **2016**, *6*, 1502104.

[48] Q. Jiang, Z. N. Chu, P. Y. Wang, X. L. Yang, H. Liu, Y. Wang, Z. G. Yin, J. L. Wu, X. W. Zhang, J. B. You, *Adv. Mater.* **2017**, *29*, 1703852.

[49] W. Chen, Y. Z. Wu, Y. F. Yue, J. Liu, W. J. Zhang, X. D. Yang, H. Chen, E. B. Bi, I. Ashraful, M. Gratzel, L. Y. Han, *Science* **2015**, *350*, 944.

[50] F. Guo, S. Qiu, J. Hu, H. Wang, B. Cai, J. Li, X. Yuan, X. Liu, K. Forberich, C. J. Brabec, Y. Mai, *Adv. Sci.* **2019**, *6*, 1901067.